Applied Catalysis A: General 479 (2014) 103–111

Contents lists available at ScienceDirect

Applied Catalysis A: General

journal homepage: www.elsevier.com/locate/apcata

Bimetallic Ag–Au/SiO_2 catalysts: Formation, structure and synergistic activity in glucose oxidation

Tímea Benkó[a,*], Andrea Beck[a], Krisztina Frey[a], Dávid Ferenc Srankó[a], Olga Geszti[b], György Sáfrán[b], Boglárka Maróti[c], Zoltán Schay[a]

[a] Centre for Energy Research, Surface Chemistry and Catalysis Department, PO Box 49, H-1525 Budapest, Hungary
[b] Research Centre for Natural Sciences, Institute for Technical Physics and Materials Science, PO Box 49, H-1525 Budapest, Hungary
[c] Centre for Energy Research, Nuclear Analysis and Radiography Department, PO Box 49, H-1525 Budapest, Hungary

ARTICLE INFO

Article history:
Received 28 January 2014
Received in revised form 1 April 2014
Accepted 13 April 2014
Available online 21 April 2014

Keywords:
Ag–Au nanoparticle
Glucose oxidation
Synergistic effect
Bimetallic catalyst
Gold catalysis

ABSTRACT

SiO_2 supported Ag–Au bimetallic catalysts were prepared by sol adsorption method with 10/90, 20/80, 33/67, and 50/50 Ag/Au molar ratios. Reduction of $HAuCl_4$ in Ag sol resulted in alloyed Ag–Au colloid particles and that structure remained after calcination and reduction treatment. The alloy structure of the catalysts was confirmed by UV–visible spectroscopy and high resolution transmission electron microscopy. The Au–Ag bimetallic effect and its dependence on the Ag/Au molar ratio was studied in glucose oxidation where synergistic activity increase was observed compared to the Au/SiO_2 reference sample in the case of the bimetallic samples with less than Ag/Au = 50/50 molar ratio. The Ag/SiO_2 was inactive at the same conditions. The Ag/Au surface atomic ratios – calculated by X-ray photoelectron spectroscopy (XPS) – were slightly higher than in the bulk—determined by prompt gamma activation analysis (PGAA). The higher activity of the bimetallic samples is suggested to be caused by the improved O_2 activating ability provided by Ag sites. The further increase of Ag loading above the optimal concentration may dilute or cover the Au to such an extent that the number of gold ensembles necessary for glucose activation decreases deteriorating the activity.

1. Introduction

Since Haruta discovered [1] the high catalytic activity of nanosize gold in CO oxidation the number of scientific papers started to grow exponentially in this field. Gold nanoparticles catalyze important reactions, such as CO oxidation, propene oxidation, water gas shift reaction, synthesis of H_2O_2, selective oxidation of alcohols and aldehydes. The activity in a desired application is determined by the oxidation state of the reactive species, the gold particle size, shape and location on the support controlled by the preparation process and the nature of the support [2,3].

First, Biella et al. published [4] the highly efficient utilization of gold catalyst in the oxidation of glucose. D-Gluconic acid is one of the most valuable oxidation products of D-glucose and used as intermediate in food and pharmaceutical industries [5]. In contrast with the Pt and Pd based catalysts (exhibiting high activity but low selectivity), using gold catalysts gluconate was obtained with 100% selectivity moreover self-poisoning and metal leaching were also avoided [6,7]. Studying the particle size and support effect of gold catalysts in our previous work an inverse correlation was found between the activities in CO oxidation and in glucose oxidation and it was demonstrated that in glucose oxidation the effect of the support is more significant than the small gold particle size [8]. Reaction mechanism suggested for glucose oxidation over gold involved O_2 reduction to hydrogen peroxide, which was experimentally detected by Rossi and coworkers. A study on the poisoning effect of different molecules on Au catalysts concluded that soft bases have high poisoning effect and hard bases (e.g. OH^-) have promoting effect on the activity in aerobic glucose oxidation. A molecular model for the electronic interactions has been suggested: soft and hard nucleophiles interact with the gold clusters in a different way and influence the oxygen reduction step of glucose oxidation [9–11].

Bimetallic catalysts appeared promising in activity enhancement in many reactions through forming new active sites and inducing synergistic effects. In oxidation reactions AgAu nanocatalysts have been reported to show synergism, higher activity has been reached in different oxygen transfer reactions such as CO oxidation, preferential CO oxidation in H_2 (PROX), oxidation of benzyl

* Corresponding author. Tel.: +36 1 392 2222 3182; fax: +36 1 392 2703.
E-mail addresses: timea.benko@energia.mta.hu, timea.benko@gmail.com (T. Benkó).

http://dx.doi.org/10.1016/j.apcata.2014.04.027
0926-860X/

alcohol and glucose. The increased activity strongly depends on the silver content of the bimetallic catalysts in CO oxidation [12], benzyl alcohol [13] and glucose oxidation [14–16]. While in the case of monometallic gold catalysts the activity is influenced by the particle size and the nature of the support, in the case of bimetallic AgAu nanoparticles (NPs) they have secondary importance in CO oxidation in presence and absence of hydrogen. [17,18]. Regarding the AgAu structure Mou et al. reported the relevance of the pretreatments: in oxidizing atmosphere Ag—O bond formation was detected by EXAFS and after reduction in H_2 the silver oxide disappears, realloying of Ag and Au was observed [18,19]. The calcination and reduction temperature also affected the catalytic activity in CO oxidation [20]. Zanella and coworkers have studied TiO_2 and SiO_2 supported Au–Ag catalysts in CO oxidation reaction and found that the support is not involved in the reaction as in the case of the monometallic gold catalysts [21]. Synergistic effect has been observed in CO oxidation between Ag and Au using mesoporous aluminosilicate as support and explained by improved adsorption and activation of oxygen on the catalysts [22]. The best activity was achieved when Ag/Au molar ratio was 3/1 and that was explained by the strongest intensity of the O_2^- species on the catalyst surface detected by electron paramagnetic resonance (EPR) technique [23].

In glucose oxidation Comotti et al. have reported [24] higher activity of activated carbon supported AuPt and AuPd nanoparticles compared to monometallic gold NPs at low pH, whereas almost no effect has been detected at pH 9.5. Hermans et al. have reported [25] synergistic activity in glucose oxidation at high pH using carbon supported Au/Pd catalysts prepared by impregnation in aqueous solution. The synergistic effect was related to high Pd surface content. Zhang, Toshima and their co-workers have extensively studied unsupported, PVP-protected bimetallic AuPd, AuPt, AgAu and trimetallic AuPtAg nanoparticles in glucose oxidation [26–31]. Synergistic activity has been reported in all three systems at high pH. The "crown-jewel-structured" AuPd nanocluster catalysts were prepared by galvanic replacement reaction method, they shown excellent activity in the reaction. The authors concluded that "the anionic charge on the top Au atoms is the direct cause for the high reactivity", based on DFT calculation results and XPS measurement; namely 0.25 eV of Au $4f_{7/2}$ binding energy decrease was detected compared to the corresponding Au nanocluster. In the case of Ag core/Au shell type bimetallic nanoparticles the highest activity was reached at Ag/Au = 1/4 atomic ratio. The synergistic activity increase was explained by the possible electronic charge transfer from Ag in the core to the Au in the shell originating from the ionization potential of Au and Ag (9.22 and 7.58 eV, respectively), however the XPS results showed binding energies corresponding to zero valence Au and Ag in the AgAu NP (Au $4f_{7/2}$: 83.8 eV and $Ag3d_{5/2}$: 367.8 eV, respectively) [14,28]. In the case of the trimetallic AuPtAg alloy NPs (atomic ratios: 70/20/10 = Au/Pt/Ag) higher activity was reported than in the case of the corresponding Au-containing bimetallic NPs and correlated to small diameter of the NPs and the negatively charged Au atoms due to electronic charge transfer from Ag atoms and the PVP stabilizer. XPS results showed the binding energy of Au $4f_{7/2}$ in the AuPtAg NPs 0.2 eV lower than that of in the pure PVP protected Au NPs (82.8 eV). DFT calculations also confirmed the negatively charged Au atoms, and Ag atoms was found positively charged in the trimetallic NPs [29,30].

As seen from the literature cited above the AgAu bimetallic NPs are very promising catalysts in oxidation reactions and the origin of their activities are not clear. Herein, we report an investigation on the formation of SiO_2 supported AgAu catalysts prepared by preformed bimetallic colloidal nanoparticles. Our aim was to produce well characterized truly bimetallic AgAu NPs of various Ag/Au atomic ratios and study the effect of particle composition on glucose oxidation activity. Application of the pre-prepared colloidal particles for the preparation ensures that the gold and silver particles are in metallic state. The structure of the AgAu colloidal particles has also been studied.

2. Experimental

2.1. Materials

Aqueous solutions of $HAuCl_4{\cdot}3H_2O$ (Aldrich); $AgNO_3$ (Aldrich); polyvinylalcohol (PVA) (Aldrich); poly(diallyldimethylammonium) chloride (PDDA) (Aldrich); commercial silica (Degussa Aerosil 200) and $NaBH_4$ (Aldrich) were used as received for the preparation of the catalysts. Analytical grade D-glucose and analytical grade Na_2CO_3 and $NaHCO_3$ for the preparation of the buffer solution were purchased from Sigma-Aldrich and used as received.

2.2. Catalyst preparation

At first bimetallic and monometallic nanoparticles stabilized by PVA in aqueous sols were prepared by reduction of $AgNO_3$ and $HAuCl_4$ precursors with $NaBH_4$, and then they were immobilized on SiO_2 support by adsorption. For formation of AgAu bimetallic nanoparticles consecutive reduction method was applied instead of co-reduction of the metal precursors in order to avoid AgCl precipitate formation during the preparation. For AgAu sols preparation different amount (2.5, 5.0, 10.0, 12.5 mL) of 6.0 mM $AgNO_3$ solution and 20 mL 0.2 wt% PVA was diluted by 400 mL Milli-Q water (resistivity: 18.2 MΩ cm at 25 °C, conductivity 0.056 μS/cm at 25 °C) produced by Millipore Water Purification Direct-Q System) and proper amount of freshly prepared 25 mM sodium borohydrid providing $BH_4^-/Ag^+ = 2$ molar ratio was added under vigorous stirring. The reduction of Ag^+ ions was indicated by the sudden appearance of yellow color that deepened during about 30 min stirring. When the Ag sol formation was completed and the $NaBH_4$ had been decomposed, the mixture of different amount (22.5, 20.0, 15.0, 12.5 mL) of 6.0 mM $HAuCl_4$ and 10 mL of 0.2 wt% PVA solution was added followed by freshly prepared 25 mM sodium borohydrid providing $BH_4^-/Au^{3+} = 2$ molar ratio. This procedure resulted samples of various Ag/Au atomic ratios: 10/90, 20/80, 33/67, 50/50. The monometallic Au and Ag sols were prepared by addition of 50 mL $NaBH_4$ solution to the mixture of 25 mL of 6.0 mM $HAuCl_4$ or $AgNO_3$ and 30 mL of 0.2 wt% PVA solutions. All the sols were prepared at 273 K in solutions cooled by icy water.

Adsorption of the above described Ag, Au and AuAg sols on SiO_2 (Aerosil 200) were assisted by PDDA addition. All suspensions were filtered, the filtered cake washed thoroughly and dried at 60 °C. Before catalytic tests the supported catalysts were calcined in synthetic air flow at 400 °C for 1 h and after that reduction treatment was carried out in hydrogen flow at 350 °C for 30 min.

2.3. Sample characterization

UV–visible absorption spectra of the sols and the supported samples were recorded at ambient temperature using a double-beam spectrophotometer (JASCO V-550). The aqueous suspensions of the catalysts samples were dropped on a glass plate and after evaporating water the UV–visible spectra of the samples were recorded.

The distribution and size of gold and silver particles on SiO_2 was studied by a Philips CM20 transmission electron microscope (TEM) operating at 200 kV equipped with energy dispersive spectrometer (EDS) for electron probe microanalysis. The gold particle size distribution was obtained by measuring the diameter of about 300 metal particles. High-resolution transmission electron microscopy (HRTEM) investigations were carried out by a JEOL 3010 microscope operating at 300 kV with a point resolution of 0.17 nm. The HRTEM was equipped with a GATAN Tridiem energy filter used for

electron energy loss spectroscopy (EELS) elemental mapping. The sols and aqueous suspensions of the samples were drop-dried on carbon-coated microgrids for the investigations. In due cases Au-etalon was dropped onto the grids and used for HRTEM reference [32].

Surface concentrations of Au and Ag were determined by X-ray photoelectron spectroscopy (XPS) performed by a KRATOS XSAM 800 XPS machine equipped with an atmospheric reaction chamber. Al *K*α characteristic X-ray line, 40 eV pass energy and FAT mode were applied for recording the XPS lines of Au 4f, Ag 3d, C 1s, O 1s and Si 2p. Si 2p binding energy at 103.3 eV was used as reference for charge compensation.

About 50–350 mg of each catalyst was analyzed with prompt-gamma activation analysis (PGAA) [33], a nuclear analytical technique for non-destructive determination of elemental compositions. This way the dissolution of the sample, any loss or contamination during the sample handling could be completely avoided. The samples were irradiated in a guided neutron beam for 5–60 000 s at the PGAA facility [34] of the Budapest Neutron Center and the gamma-rays from the radiative neutron capture are detected with a Compton-suppressed HPGe detector. The energies and intensities of the peaks in the gamma spectrum were determined with the Hypermet-PC [35] program, whereas the element identification and the calculation of the concentrations was done with the program ProSpeRo [36], utilizing our prompt-gamma analysis library [37]. Every step of the measurement and the evaluation can be described with statistical methods; therefore the uncertainties of the results can be readily estimated from a single measurement.

2.4. Catalytic test

The catalytic behavior of the samples was evaluated in glucose oxidation as a model reaction. Oxidation of glucose was carried out in a thermostated, magnetically stirred batch reactor, bubbling oxygen at atmospheric pressure through the liquid phase. The reaction was started by adding the calcined (400 °C in air for 1 h) or calcined then reduced (350 °C in H_2 for 30 min) catalyst to the O_2 saturated solution. pH was kept at a constant value 9.5 by using carbonate-bicarbonate (volume ratio: 2:3) buffer solution. Typical reaction parameters were: c_{buffer} = 0.1 M, T = 35 °C stirring rate = 1000 rpm, $c_{glucose}$ = 0.1 M in 30 mL water solution, O_2 flow = 100 mL/min (1 atm).

HPLC on a JASCO instrument equipped with a Jasco UV 2075 and an ERC 7515A RI detector. A Hamilton HC-75H+ form cation exchange column was used with aqueous succinic acid 0.11 mM as the eluent with 0.4 mL/min flowing rate was applied to measure the concentration of glucose and gluconic acid. The conversion was calculated on the basis of the concentration of gluconic acid produced and glucose consumed. Under these conditions selectivity was always 100%.

3. Results and discussion

3.1. Formation of Ag–Au nanostructures

In order to understand the structure of the catalysts, characterization of the system was carried out at each step of the preparation process.

In the first step PVA stabilized Ag sol was formed by reducing $AgNO_3$ with $NaBH_4$. This parent Ag sol was analyzed by HRTEM which provided information on the crystal structure of the sample. Considering our preparation method regular cubic Ag crystal structure was expected. In fact, we have found particles of both fcc and hexagonal structures. Fig. 1 shows a HRTEM image of the

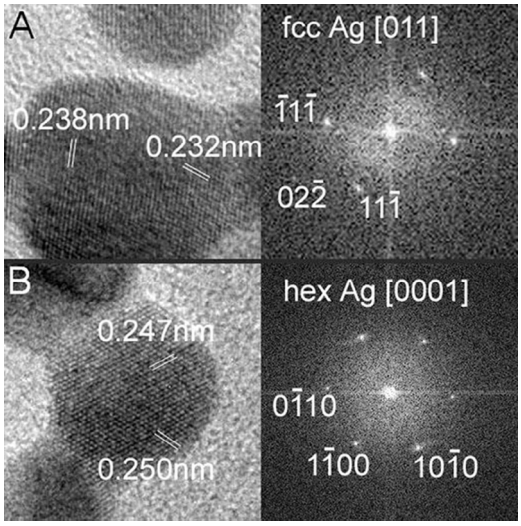

Fig. 1. HRTEM image of the Ag sol. The particles marked with A and B with corresponding FFT patterns represent fcc and hexagonal Ag phases, respectively.

Ag sol. We measured the lattice fringes in numerous grains and found distances of 0.250 nm, 0.247 nm, 0.238 nm and 0.232 nm. The 0.238 nm and 0.232 nm lattice periods and the 70.5° interplanar angle measured in particle A refers to the (1 1 1) planes of the usual face centered cubic phase (PCPDF 040-783) as indicated also in the fast Fourier transform (FFT) inset of A. However, in particle B we measured fringe spacings of 0.250 nm and 0.247 nm with an interplanar angle of 60°, that cannot be indexed with fcc structure. Instead, these lattice spacings at an angle of 60° can be indexed as the (10–10) type planes of the hexagonal 4*H*-Ag structure (PCPDF 411-402) as represented also in the FFT inset in Fig. 1(B) Selected area electron diffraction (SAED) results confirm the coexistence of the Ag-fcc and Ag-4*H* in same extent in the Ag sol. Such coexistence was also observed in the case of Ag-nanowires [38]. The equilibrium crystal structure for silver is fcc (a = 0.4086 nm) [39], however, three other polytypes of Ag have also been reported: the 9R polytype forming at grain boundaries in polycrystalline Ag, [40], the two-dimensional (2*H*) hexagonal phase of Ag can be grown on glass and Si by controlled electrochemical deposition [39] and the 4*H* hexagonal polytype which, interestingly, to date, has been observed only in nanocrystalline and continuous films [39,41] or nanorods [38,42,43].

Size-dependent phase stability of silver nanocrystals governing the formation of different Ag polytypes was reported in Refs. [38,44]. Chakraborty et al. [39] underlined the importance of the control of growth kinetics prior to the size effect and concluded that the former is enough to obtain any of the three polytypes of Ag. Huang et al. [45] successfully fabricated belt-like 4*H* Ag and suggested that the reason why 4*H* Ag is rarely observed is probably due to a special combination of synthesis parameters. Similar interpretation of why 4*H* Ag is favored under our experimental condition could be applied. In our preparation method the silver nanoparticles were prepared in aqueous media and $NaBH_4$ was added quickly to the mixture of $AgNO_3$ and PVA. The reduction of the Ag ions happened rapidly. Thermodynamically the fcc structure is favorable while under kinetic control the less stable 4*H* hexagonal polytype of silver can be grown. For 4*H* Ag higher chemical activity is supposed because of its higher distance between the planes than in fcc structure Ag. Our simple Ag sol preparation process could be a basis for synthetizing Ag nanoparticles with desired polymorph.

HRTEM provided further information on the structure of the bimetallic sol sample prepared by $HAuCl_4$ reduction in the parent Ag sol. A HRTEM image of the bimetallic 33Ag67Au sol is shown in

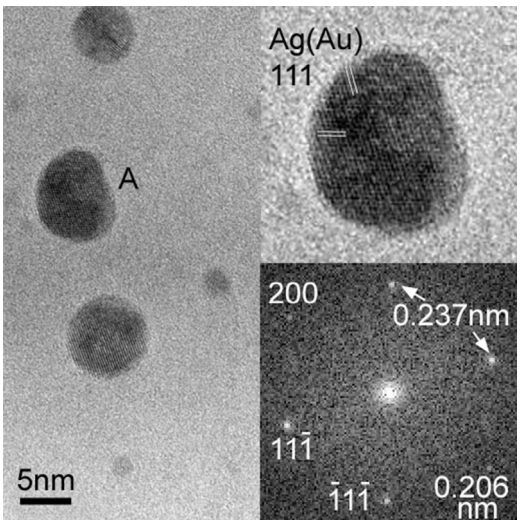

Fig. 2. HRTEM image of 33Ag67Au sol with the inset of the enlarged particle marked with A and the inset of its FFT pattern. The 0.237 nm lattice periods at an angle of 71° and the 0.206 nm-period at an additional angle of 54°, correspond to the (1 1 1) and (2 0 0) planes of fcc Ag(Au), respectively.

Fig. 2. The enlarged image and the FFT pattern of particle A (insets) show lattice periods and reflections of 0.237 nm and 0.206 nm positioned at an angle of 71° and 54°, respectively. That obviously refers to the (1 1 1) and (2 0 0) planes of fcc Ag(Au) structure as shown by the corresponding indices in the FFT. Contrarily to the 4*H* of Ag sol, the fcc Ag(Au) structure was found typical in the bimetallic AgAu system.

The contrast features of the particles in the micrograph suggest that Ag and Au are randomly distributed, i.e. Ag(Au) alloy formation. It is to mention, that in case of 6 nm-size Au–Pd particles concentric dark/bright contrast could be detected by TEM in our laboratory, earlier, indicating Au_{core}–Pd_{shell} structure [46]. Hodak et al. have shown clear phase boundaries between the Au core and the Ag shell for particles ≥20 nm, but for particles with smaller sizes phase contrast were not observed. Size-dependent spontaneous alloy formation was concluded by Shibata et al. [47]. In the case of alloy structures, e.g. Cu–Au [48], Zn–Au [49], Pb–Au [46,50], Sb–Au [51] HRTEM is utilized to determine the change in the lattice parameters resulting from the alloying process. Gold and silver have similar atomic sizes and a face centered cubic (fcc) crystal structure with similar lattice constants of 0.408 nm and 0.409 nm, respectively [47]; complete miscibility can be obtained by these metals in the bulk at any composition with no change in lattice constants. Therefore the usually observed lattice parameter change in the case of alloy structures is not expected in Ag–Au system. 4*H* Ag hexagonal crystal structure – found in the case of the parent Ag sol – was not detected in the case of alloy sol samples, only the equilibrium fcc crystal structure was observed. The absence of 4*H* Ag phase in the alloy could be due to that the NPs can be restructured during the preparation process.

Fig. 3A–C shows the unfiltered TEM image of bimetallic 33Ag67Au, the EELS Ag elemental map of the same area and the plasmon image of the sample sol, respectively. The bright contrast in the Ag map (b) refers to high Ag concentration that indicates the presence of Ag in all particles. Particles smaller than 2 nm cannot be seen in the Ag map because of the ambient noise. We can conclude that every – observable – particle contains Ag, so the particles should be bimetallic. Alloy formation is supported also by the contrast within the particles that is distinct from the appearance of core–shell structure in bimetallic particles.

The plasmon image shows dark contrast of the catalyst particles compared to the non-metallic carbon background. That represents metallic feature of the Ag–Au particles suggesting that all of them are reduced.

UV–visible spectra of the AgAu nanostructures were recorded to understand the formation of the bimetallic particles. Fig. 4a–d shows the baseline corrected absorption curves of (a) the parent Ag sol; (b) the bimetallic 20Ag80Au sol; (c) the mixture of the monometallic Ag and Au sol in 20/80 volume ratio and (d) Au sol prepared by the same way as all of the other sols (see in Section 2.2). The inset shows the original spectra of the sols. As shown in Fig. 4 the Au surface plasmon resonance (SPR) appeared at 520 nm and the Ag SPR at 408 nm. The origin of this surface plasmon band is the collective oscillations of free conduction electrons in metal excited by light at a particular wavelength [52]. In the case of the AgAu bimetallic sol a single absorption band appeared at 503 nm.

In order to check the possibility of the formation of separate monometallic particles during the synthesis of AgAu sol, a mixture of Ag and Au monometallic sols were used as a blank experiment. In the case of the mixture sol two distinct surface plasmon bands appeared at 406 nm and 523 nm. The results proved that bimetallic AgAu sol formed and not a mixture of Au and Ag sols. The disappearance of Ag SPR and blue shift of Au SPR suggests that the Au reduced on the surface of Ag. This results proved that the $[AuCl_4]^-$ anion is able to replace the PVA on the surface of the Ag particle and the reduction of Au^{3+} takes place there. According to our preparation process the consecutive reduction of the silver and gold ions should led to Ag-core Au-shell particles, but the single band for the bimetallic particles suggests AgAu alloy formation in the sol, which is in agreement with HRTEM results. Nonalloy, or core–shell Au–Ag nanoparticles, exhibit two characteristic absorbance peaks [53]. According to theoretical calculations (based on Mie theory) in the case of core–shell structure, gold deposition should result only in damping of the underlying silver surface plasmon band.

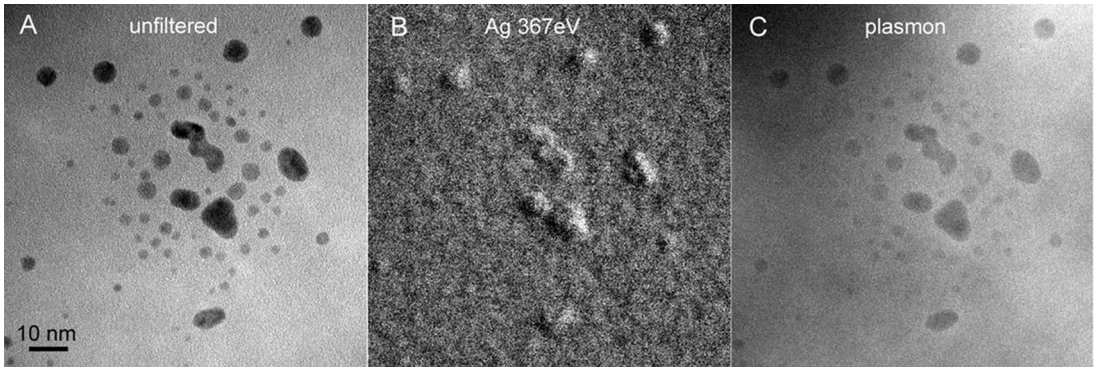

Fig. 3. (A) TEM image of the of bimetallic 33Ag67Au sol sample, (B) EELS Ag elemental map and (C) plasmon image of the same area.

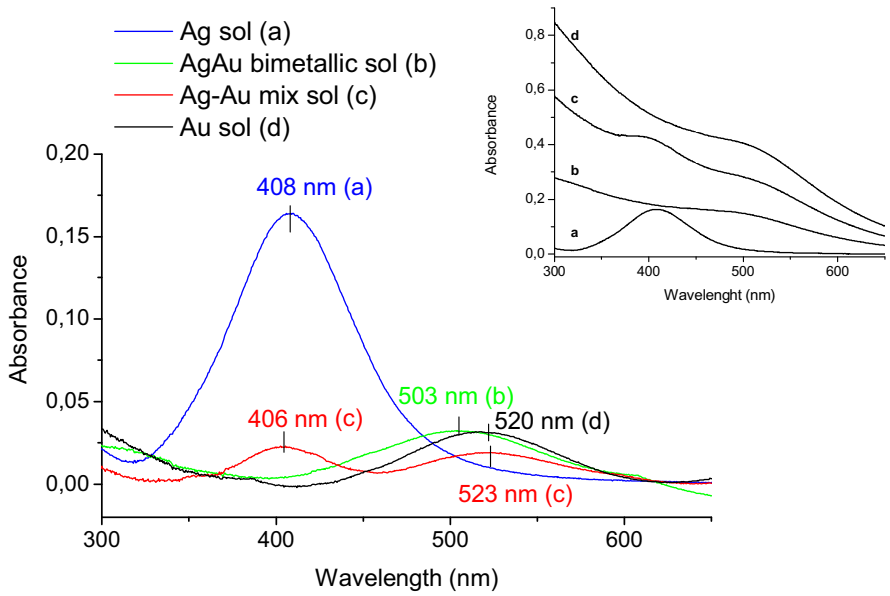

Fig. 4. UV–visible spectra of (a) Ag sol; (b) the bimetallic 20Ag80Au sol, (c) the mixture of the monometallic Ag and Au sol in 20/80 volume ratio and (d) Au sol after linear baseline corrections. The inset shows the original spectra of the same sols.

The blue shift of single Au SPR can correlated with alloy structure and originated from the perturbation of the d-band energy levels [54].

Considering the electrode potential of the metals in the system, it is clear that its relations favor the alloy formation. Ag was in metallic form when Au^{3+} ions were added to the system. $Ag + Au^{3+} \rightarrow Ag^{+} + Au$ reaction could take place thus the reduction of Au^{3+} was caused by both the BH^{4-} reducing agent and the Ag; and simultaneously the Ag^{+} formed was reduced by $NaBH_4$, which promoted the intermixing of the metals. The reduction of Au precursor by metallic Ag was confirmed in a separate experiment, when solution of $HAuCl_4$ and PVA was added to the Ag sol without $NaBH_4$ reducing agent. The sudden disappearance of the yellow color of the Ag sol and the slow evolution of the red color of the bimetallic sol indicated that galvanic replacement reaction took place.

Shibata et al. also observed [47] spontaneous alloying of bimetallic core–shell Au–Ag nanoparticles at ambient temperature, which was explained by the vacancy defects at the boundary between the two metals. Such defects may be caused by the need to replace the stabilizers at the surface of the particle during synthesis of the shell. In our case similar behavior could also be the reason of the alloy formation in the sol. The diffusion of metals is commonly accepted to proceed via migration of atoms into vacancy defects. A single vacancy at the interface is enough to catalyze fast diffusion. This process is reinforced by the decreased melting point of the metals due to small diameter of the particles [54].

3.2. Structure of the AgAu/SiO_2 catalysts

The actual metal contents and the Ag/Au ratios of the catalysts were determined by prompt gamma activation analysis (PGAA), and fit well with the nominal values (Table 1.)

Table 1 presents AgAu particle sizes of the catalyst samples after calcination at 400 °C in synthetic air (by that the organic residues can be removed) and after following reductive treatment in H_2 at 350 °C determined by TEM and the standard deviations which are characteristic of the particle size distribution. The mean particle size of pure Au/SiO_2 and pure Ag/SiO_2 sample were similar, 4.8 nm. In the case of Ag/SiO_2 sample the particle size distribution was broad (4.8 ± 3.5 nm) due to several much larger particles with 5–16 nm in diameter beside the numerous particles with 3–4 nm size. In the case of the bimetallic samples the mean particle sizes range between 2.9 and 5.2 nm. In the case of Au/SiO_2 the decreased Au particle size after reduction is surprising. Small changes were observed in the particle sizes after reduction treatments (or catalytic reaction), and the resulting sizes were more similar in the different samples than in the calcined state.

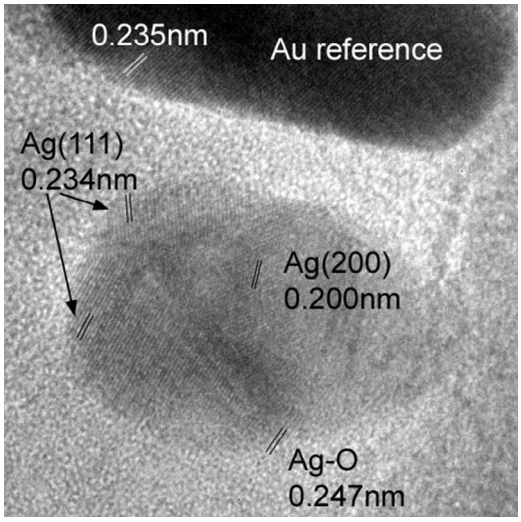

Fig. 5. HRTEM of Ag/SiO_2 calcined at 400 °C. The 0.200 nm and 0.234 nm fringe periods represent metallic fcc Ag phase. The 0.247 nm period represent Ag-oxide.

HRTEM of monometallic calcined Ag/SiO_2 sample is shown in Fig. 5. Fringe periods of both Ag (0.200 nm and 0.234 nm) and Ag_2O_3 (0.247 nm, PCPDF 72-0607) can be identified in the catalyst particle after calcination in air at 400 °C. The precision of this measurement was provided by a comparison with the (1 1 1) lattice spacings (0.235 nm) of the Au reference particle visible at the top of Fig. 5. Only a few crystals were found as pure silver-oxide, most part of the particles was in metallic phase. It is worth pointing out that both Ag and Ag-oxide phases were present within one particle (Fig. 5) regardless of the size of the particles in every case where Ag-oxide was observed. HRTEM measurement of 33Ag67Au/SiO_2 bimetallic catalyst showed mostly metallic Ag(Au) crystals and two-phase contrast was not seen within the particles.

Table 1
Metal content and particle sizes of the catalysts determined by PGAA and TEM, respectively.

Catalysts	Ag/Au (%)	Metal content		Particle size (nm)	
		Ag (mmol/g_{cat})	Au (mmol/g_{cat})	After calcination	After reduction
Au/SiO_2	0/100	0	0.190	4.8 ± 2.4	4.0 ± 2.0
$10Ag90Au/SiO_2$	13/87	0.014	0.093	3.5 ± 2.3	3.1 ± 1.6 (3.5 ± 2.0*)
$20Ag80Au/SiO_2$	23/78	0.025	0.085	2.9 ± 1.2	3.5 ± 1.7
$33Ag67Au/SiO_2$	33/67	0.033	0.067	3.4 ± 2.5	3.3 ± 1.2
$50Ag50Au/SiO_2$	51/49	0.049	0.051	5.2 ± 2.2	–
Ag/SiO_2	100/0	0.092	0	4.8 ± 3.5	4.9 ± 3.6

* Particle size after catalytic reaction.

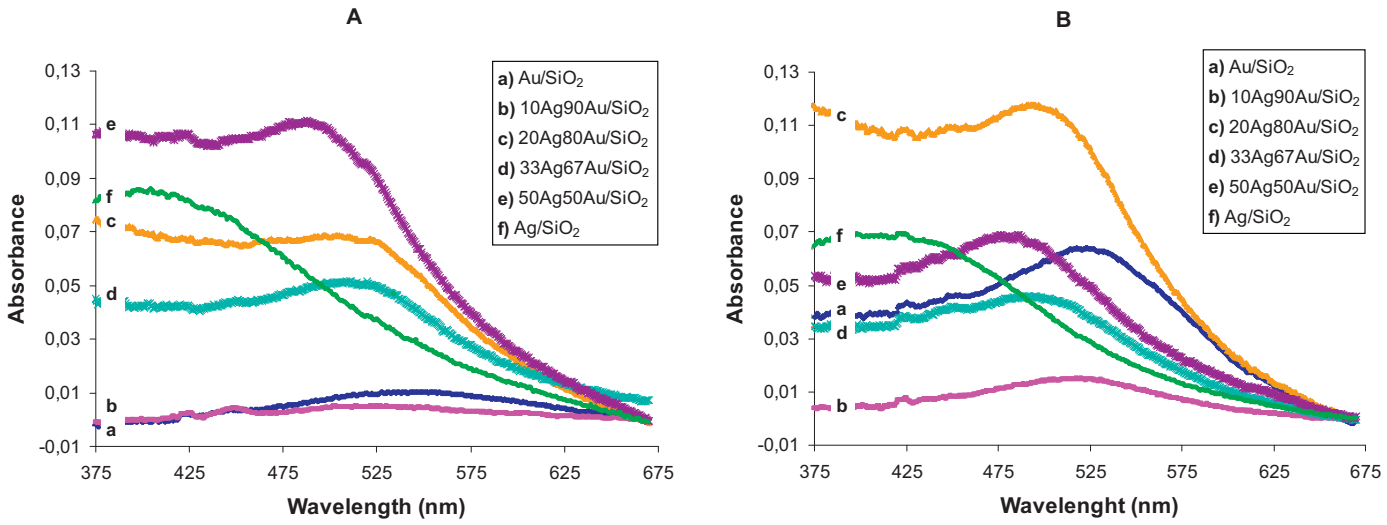

Fig. 6. UV–visible spectra of $AgAu/SiO_2$ catalysts after calcination in air at 400 °C (A), after reduction in H_2 at 350 °C (B).

Fig. 6 shows the UV–visible spectra of the supported catalysts after calcination (A) and after reduction treatment (B). The intensities of the bands are not comparable because – as a consequence of the measurement method – the catalyst amounts placed on the glass plates were not the same.

Single adsorption bands were detected in the case of all samples after calcination. All surface plasmon resonance (SPR) bands were broad due to the size distribution of the particles. After reduction only single, narrower SPR bands were detected for all catalysts compared to the bands of the calcined samples.

Fig. 7 shows the correlation between the nominal Au molar ratio and the maximum of surface plasmon bands. The SPR bands shift to higher wavelengths with increasing Au molar ratio. The position of the maximum absorption band is related to the surface structure and composition beside the particle size [22,28]. In accordance with the literature linear correlation was found in the case of calcined samples and reduced samples showing Ag–Au alloy structure.

In a recent study [55] on the dependence of the SPR band on the alloy composition the authors found that the correlation between the position of the SPR band and the gold fraction was deviated from linearity and was described by a third-order polynomial function. The composition dependence can be approached by a linear relation between 0.2 and 0.8 gold fraction range only. The authors took into account alloy nanoparticles with diameters between 5 nm and 50 nm as against our work where smaller than 5 nm sized particles were studied. The band positions were changed with calcination-reduction treatments in our case. In the calcined samples deviation from linearity can be originated from the somewhat different particle size and may suggest some phase segregation, inhomogeneity of alloy. Reduction pretreatment caused a blue shift of the absorption bands and a diminution of the deviation from linearity suggesting more homogeneous AgAu alloy structures. This effect could be explained by the following: oxygen treatment favors the Ag concentration enhancement on the surface because Ag-oxide formation is thermodynamically favored, but as the temperature raises the decomposition of the preformed oxide is occurred above 250 °C [56]. Modification of the surface plasmon of the particles

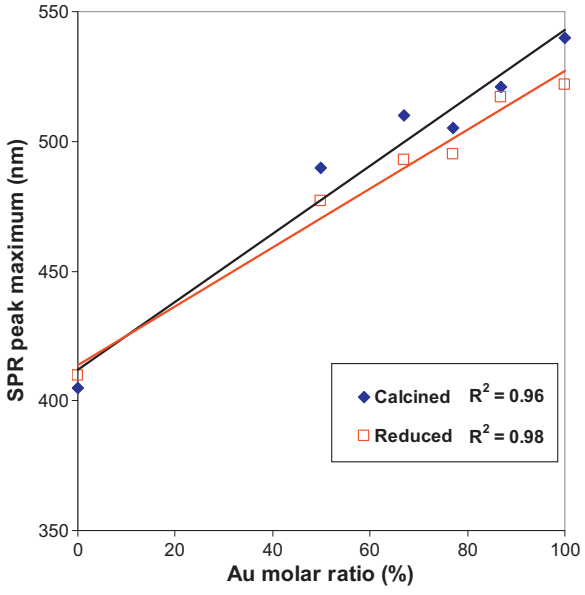

Fig. 7. UV–visible absorption band maximum of $AgAu/SiO_2$ catalysts versus Au molar fraction after calcination in air at 400 °C and reduction in H_2 at 350 °C.

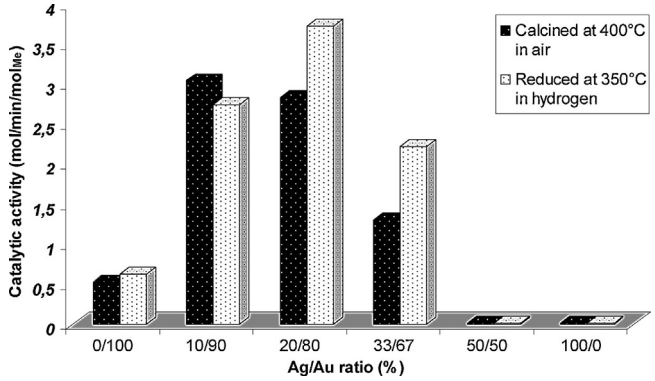

Fig. 8. Catalytic activities of the AgAu/SiO_2 samples in glucose oxidation; T = 35 °C, pH 9.5, $c_{glucose}$ = 0.1 M.

likely reflects this surface structure/geometry change, that can be an important factor affecting the catalytic properties.

The results confirm that the AgAu nanoparticles prepared by our method are AgAu alloy with random distribution of Ag atoms rather than core–shell AgAu, AuAg or a mixture of Au and Ag nanoparticles [12].

To determine the oxidation states of the bimetallic nanoparticles close to the surface and the relative surface concentration of Ag and Au XPS spectra were recorded on the catalyst samples after calcination in air at 400 °C and after reduction treatment in H_2 at 350 °C. Table 2 shows the binding energies of Au $4f_{7/2}$ and Ag $3d_{5/2}$. (The corresponding graphs can be found in the online Supplementary materials). BE of Au was in the range of 82.9–83.2 eV which can be assigned to Au metallic state. Combining Au with Ag the BE of Ag shifts to lower value (366.8–367.5 eV) from 368.6 eV measured for calcined Ag/SiO_2 sample. The effect of reduction treatment on the BE was smaller and not really significant in the case of bimetallic catalysts than in the case of pure Ag/SiO_2, in case of that the BE of Ag $3d_{5/2}$ decreased by 1.4 eV.

However, the clear shift of Ag $3d_{5/2}$ band to lower BE in the monometallic Ag/SiO_2 as a result of reducing treatment is in contradiction with the general view about behavior of Ag (according to the literature the BE of Ag $3d_{5/2}$ for metallic Ag is 368.3 eV, while for oxidized Ag varies between 367.3–368.0 eV) and our other results. Further experiments are in progress to clarify this unusual behavior of Ag.

The surface atomic ratio of Ag and Au were calculated using sensitivity factors given by the manufacturer and are presented in Table 2. Surface Ag/Au ratios are only slightly higher than the bulk for the 10Ag90Au/SiO_2 and 20Ag80Au/SiO_2 catalysts, but high Ag enrichment on the surface was observed for the 33Ag67Au/SiO_2.

3.3. Catalytic properties

The bimetallic Ag–Au/SiO_2 catalysts with different Ag–Au ratios were tested in glucose oxidation. The catalytic activity of the samples was compared in Fig. 8. Synergistic activity increase was achieved with addition of Ag to Au at lower than Ag/Au = 50/50 nominal atomic ratio. Regarding that the mean particle size of the bimetallic particles is the smallest (2.9 nm) in the 20Ag80Au/SiO_2 sample; it does not mean that the 20/80 is the optimum atomic ratio. At 50% nominal Ag content no activity was detected as in the case of pure Ag/SiO_2 sample. The inactivity of 50Ag50Au/SiO_2 cannot be explained only by the different particle size (5.2 nm), the Ag/Au ratio must be a more important factor. Taking into account that the penetration depth of XPS is greater than one monolayer it is possible that the Ag/Au atomic ratios are higher in the topmost surface layer than the XPS results show and this causes the inactivity of the 50Ag50Au/SiO_2 sample.

The effect of the reduction treatment in H_2 at 350 °C of the calcined samples was investigated. The activity reached a maximum value at 20/80 Ag/Au ratio in the case of the reduced sample. The reduction treatment slightly affects the activity of the calcined 10Ag90Au/SiO_2 and Au/SiO_2 catalysts, while the particle size decreased somewhat. The 50Ag50Au/SiO_2 and Ag/SiO_2 showed no activity even in reduced form. The reduction treatment increased the activity to a higher extent in the case of 33Ag67Au/SiO_2 and somewhat lower extent in the case of 20Ag80Au/SiO_2, These differences might be explained by the decreased surface Ag/Au atomic ratio in the latter reduced (Table 2) samples compared to the calcined ones, supposing that the optimal Ag/Au surface ratio (at which the activity reached the maximum value) is lower than in calcined 20Ag80Au/SiO_2.

Physical mixture of the monometallic Ag/SiO_2 and Au/SiO_2 catalysts in 20% and 80% metal content, respectively, was also tested in the reaction. The activity correlated to the activity of the monometallic Au/SiO_2 as converted to the same amount of metal. Absence of any synergistic effect shows that the Ag of the physical mixture is not involved in the reaction.

The stability of the catalysts in the reaction was tested with the used calcined 10Ag90Au/SiO_2 catalyst. The activity of that sample was high, but decreased somewhat compared to the fresh sample. The reason of the activity-decrease is under investigation.

3.4. The role of Ag

The higher activity of the bimetallic samples can be originated from the role of Ag in the oxygen activation during the reaction. Alloying silver with gold induces significant changes in the mode of oxygen adsorption on Ag. Kondarides and Verykios studied [57] the oxygen adsorption properties of α-Al_2O_3 supported silver–gold alloy catalysts using micro-gravimetric and temperature desorption techniques in the temperature range from 30 to 400 °C. Three types of adsorbed oxygen species have been proposed on the alloy surface including molecular, atomic and subsurface. Subsurface oxygen diffusion, which is initiated at relatively high adsorption temperatures, inhibited by the presence of Au in the AgAu alloy. The population of atomic oxygen decreases with increasing Au content because of the need of silver multiatom adsorption sites for atomic oxygen adsorption. On pure Au surfaces the dissociative adsorption of O_2 is limited, particle morphology is a key factor influencing O_2 dissociation, it is more favored on low coordinated corner and edge Au atoms highly populated on small particles of about less than 2 nm diameter [1,58–60]. In the Ag–Au alloy molecular oxygen adsorption is favored due to the absence of Ag multiatom sites and the presence of single Ag atoms. In our experimental conditions (at high Au and low Ag content, low temperature, aqueous media) molecular adsorption could take place on the surface of bimetallic catalysts. The high surface coverage of hydroxide ions in water at high pH also makes difficulties in oxygen dissociation therefore atomic oxygen adsorption is not likely on the surface of our catalysts.

Considering the ionization potential of Au and Ag is 9.22 and 7.58 eV, respectively; electronic charges could transfer from Ag to Au atoms, but in the case of our bimetallic samples the BE of Au (or Ag) did not depend on the Ag/Au molar ratio. Experimental results with the physical mixture of the monometallic catalysts (no synergistic activity increase was detected in that case) suggested that synergism occurred if Ag atoms were in the vicinity of Au atoms, maximum activity was reached at Ag/Au = 20/80. The Ag/Au ratio affected the geometry (size, shape and surface composition) of the particles. Considering the molecular size of glucose (1 nm of diameter [61]) and Ag (or Au) atoms (atomic radius 0.144 nm), the former

Table 2
XPS data of $AgAu/SiO_2$ catalysts.

Catalysts	Au binding energy (eV)		Ag binding energy (eV)		Ag/Au atomic ratio		
					Bulk[a]	Surface	
	Calcined catalysts	Reduced catalysts	Calcined catalysts	Reduced catalysts		Calcined catalysts	Reduced catalysts
Au/SiO_2	83.0	83.0	–	–	–	–	–
$10Ag90Au/SiO_2$	82.9	82.8	367.0	366.8	0.15	0.18	0.17
$20Ag80Au/SiO_2$	82.9	82.8	367.5	367.3	0.29	0.34	0.28
$33Ag67Au/SiO_2$	82.9	83.2	367.0	367.1	0.49	1.14	1.00
$50Ag50Au/SiO_2$	82.9	83.1	367.4	367.3	0.95	1.17	1.17
Ag/SiO_2	–	–	368.6	367.2	–	–	–

[a] Determined by PGAA.

is much larger than the latter. Consequently for glucose activation multiatom adsorption sites are needed. Considering the size of glucose, oxygen and gold/silver atoms, more space is needed for the surface adsorption of the glucose than the O_2. Oxygen adsorption is preferred on silver rather than on gold and adsorption of other negatively charged species (OH groups, carbonate and bicarbonate species) may be stronger on the positively charged Ag than on Au. The strength of adsorption of these molecules on gold is thought to be weaker compared to silver, therefore the glucose may substitute the pre-adsorbed molecules on the gold surface but not on the silver surface. Thus the O_2, OH adsorption is suggested to be dominant on Ag sites, while glucose adsorption on multiatom Au sites and the reaction takes place between these species in close vicinity. If the Ag/Au ratio is higher than the ideal one, the adsorption of larger glucose is hindered also on gold. Having not enough extended Au surface lowers the glucose oxidation activity.

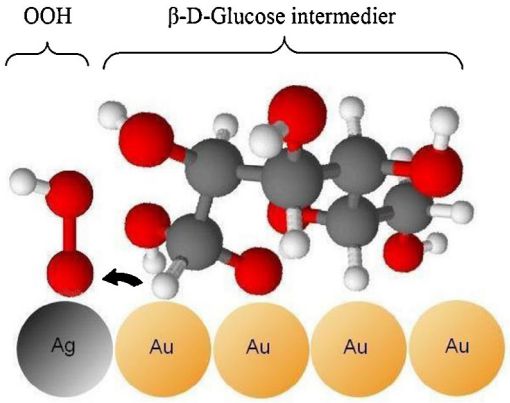

Fig. 9. Schematic illustration of the reaction between the adsorbed peroxide and the glucose intermedier (3) on the catalysts surface.

3.5. Hypothetical reaction mechanism

The mechanism proposed for glucose oxidation over our silica supported silver–gold catalysts is consistent with our experimental results and based on previous studies for alcohol oxidation [62] and glucose oxidation on gold catalysts [9,11,63].

Zope et al. have studied [62] the oxidation of alcohols over Au/C catalyst with isotopically labeled O_2 and $H_2{}^{18}O$ in order to clarify the origin of oxygen in the product and found that O is originated from hydroxide ions instead of molecular oxygen. Molecular oxygen is thought to be take part in the reaction by regeneration of the hydroxide through hydrogen-peroxide formation and dissociation and by removal of the electrons left on the surface by the OH^- adsorption. The following reaction steps have been suggested (* refers to the surface of the catalyst):

$$[O_2]^* + [H_2O]^* \rightarrow [OOH]^* + [OH]^* \quad (1)$$

$$[OOH]^* + [H_2O]^* \rightarrow [HOOH]^* + [HO]^* \quad (2)$$

$$[HOOH]^* \rightarrow [OH]^* + [OH]^* \quad (3)$$

$$[OH]^* + e^- \leftrightarrow OH^- + ^* \quad (4)$$

Density functional theory calculations [62] on ethanol oxidation over gold surfaces showed the highest activation barriers for the decomposition of peroxide (2) and hydrogen peroxide (3) intermediates. All the other reaction steps showed lower activation barriers.

Study on the decomposition of hydrogen peroxide on silver, gold and silver-gold alloys concluded high activity of silver in this reaction compared to gold [64]. Inspite of the activity-reducing effect of gold addition to silver, the alloy showed higher activity than pure gold.

Scheme 1 shows the suggested reaction scheme for glucose oxidation over our bimetallic $AgAu/SiO_2$ catalysts. The glucose adsorbs on the catalysts surface and forms alkoxy intermediate of the geminal diol with adsorbed hydroxide, which is followed by the subsequent elimination of H^+ by the HOO species adsorbed on Ag (5). This helps the decomposition of the HOOH on silver. The active center of the catalyst should contain Ag and Au in low Ag/Au ratio, where the adsorbed OOH and glucose intermedier (3) are close enough to each other to react. Fig. 9 shows the schematic illustration of the active center of the catalyst with the reaction between the adsorbed OOH and glucose.

$$[OOH]_{surf.Ag} + [RCH(OH)O]_{surf.Au} \rightarrow [HOOH]_{surf.Ag} + [RCOOH]_{surf.Au} \quad (5)$$

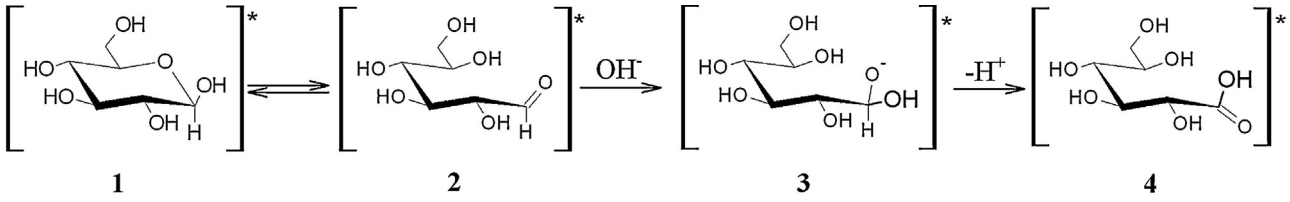

Scheme 1. Suggested reaction scheme for glucose oxidation over $AgAu/SiO_2$ bimetallic catalysts.

The higher activity of our bimetallic samples compared to the monometallic Au/SiO_2 catalyst can be explained by the higher decomposition rate of peroxide-species on the surface of the bimetallic catalysts promoted by Ag. Geometry of the metal surface plays an important role in the creation of the active centers.

4. Conclusion

Summarizing, Ag addition to Au/SiO_2 up to about Ag/Au = 33/67 provided synergetic effect in selective glucose oxidation reaction. The AgAu catalysts contained dominantly alloyed metallic particles both after calcination and following reduction treatments. The calcination–reduction pretreatment changing somewhat the particle size and the surface Ag/Au atomic ratio slightly affected the activity of the catalysts, however, the activity order of the samples remained the same. The higher activity of the bimetallic samples could be due to the improved O_2 activating ability provided by Ag sites at optimum surface arrangement The further increase of Ag loading above the ideal concentration may dilute or cover the Au to such an extent that the number of gold ensembles necessary for glucose activation decreases deteriorating the activity.

Acknowledgments

The authors dedicate this paper to the memory of Professor László Guczi, the late head of their research group. The work of Timea Benkó was supported by the European Union and the State of Hungary, co-financed by the European Social Fund in the framework of TÁMOP-4.2.4.A/2-11/1-2012-0001 'National Excellence Program'. The authors are indebted to Dr. Anita Horváth, Dr. László Borkó and Professor Antal Tungler and for valuable discussion and helpful suggestions. The research was supported by the Hungarian Science and Research Fund (OTKA K101854, OTKA K101897, OTKA NNF2-85631).

Appendix A. Supplementary data

Supplementary data associated with this article can be found, in the online version, at http://dx.doi.org/10.1016/j.apcata.2014.04.027.

References

[1] M. Haruta, N. Yamada, T. Kobayashi, S. Iijima, J. Catal. 115 (1989) 301–309.
[2] G.C. Bond, C. Luis, D.T. Thompson, Catalysis by Gold, in: Catalytic Science Series Imperial, vol. 6, Imperial College Press, London, 2006.
[3] T. Mallat, A. Baiker, Annu. Rev. Chem. Biomol. Eng. 3 (2012) 11–28.
[4] S. Biella, L. Prati, M. Rossi, J. Catal. 206 (2002) 242–247.
[5] A.P. Rauter, P. Vogel, Y. Queneau, Topics in Current Chemistry, in: Carbohydrates in Sustainable Development II, 295, Springer, Berlin, Heidelberg, 2010, pp. 63–92.
[6] M. Besson, F. Lahmer, P. Gallezot, G. Fleche, J. Catal. 152 (1995) 116–121.
[7] M. Besson, P. Gallezot, Catal. Today 57 (2000) 127–141.
[8] T. Benkó, A. Beck, O. Geszti, R. Katona, A. Tungler, K. Frey, L. Guczi, Z. Schay, Appl. Catal., A: Gen. 388 (2010) 31–36.
[9] C. Della Pina, E. Falletta, M. Rossi, Chem. Soc. Rev. 41 (2012) 350–369.
[10] C. Della Pina, E. Falletta, M. Rossi, A. Sacco, J. Catal. 263 (2009) 92–97.
[11] M. Comotti, C. Della Pina, E. Falletta, M. Rossi, Adv. Synth. Catal. 348 (2006) 313–316.
[12] Y. Iizuka, A. Kawamoto, K. Akita, M. Daté, S. Tsubota, M. Okumura, M. Haruta, Catal. Lett. 97 (3–4) (2004) 203–208.
[13] X. Huang, X. Wang, X. Wang, X. Wang, M. Tan, W. Ding, X. Lu, J. Catal. 301 (2013) 217–226.
[14] S. Tokonami, N. Morita, K. Takasaki, N. Toshima, J. Phys. Chem. C 114 (2010) 10336–10341.
[15] M.C. Daniel, D. Astruc, Chem. Rev. 104 (2004) 293–346.
[16] H. Shi, L. Zhang, W. Cai, J. Appl. Phys. 87 (3) (2000) 1572–1574.
[17] X. Liu, A. Wang, L. Li, T. Zhang, C.Y. Mou, J.F. Lee, Prog. Nat. Sci. Mat. Int. 23 (3) (2013) 317–325.
[18] A. Wang, X.Y. Liu, C.Y. Mou, T. Zhang, J. Catal. 308 (2013) 258–271.
[19] C.W. Yen, M.L. Lin, A. Wang, S.A. Chen, J.M. Chen, C.Y. Mou, J. Phys. Chem. C 113 (2009) 17831–17839.
[20] Z. Qu, Guozhou Ke, Y. Wang, M. Liu, T. Jiang, J. Gao, Appl. Surf. Sci. 277 (2013) 293–301.
[21] A. Sandoval, A. Aguilar, C. Louis, A. Traverse, R. Zanella, J. Catal. 281 (2011) 40–49.
[22] A.Q. Wang, C.M. Chang, C.Y. Mou, J. Phys. Chem. B 109 (2005) 18860–18867.
[23] A.Q. Wang, J.H. Liu, S.D. Lin, T.S. Lin, C.Y. Mou, J. Catal. 233 (2005) 186–197.
[24] M. Comotti, C. Della Pina, M. Rossi, J. Mol. Catal. A: Chem. 251 (2006) 89–92.
[25] S. Hermans, A. Deffernez, M. Devillers, Catal. Today 157 (2010) 77–82.
[26] H. Zhang, T. Watanabe, M. Okumara, M. Haruta, N. Toshima, Nat. Mater. 11 (2012) 49–52.
[27] H. Zhang, N. Toshima, J. Colloid Interface Sci. 394 (2013) 166–176.
[28] H. Zhang, N. Toshima, Appl. Catal., A: Gen. 447–448 (2012) 81–88.
[29] H. Zhang, M. Okumura, N. Toshima, J. Phys. Chem. C 115 (2011) 14883–14891.
[30] H. Zhang, N. Toshima, Appl. Catal., A: Gen. 400 (2011) 9–13.
[31] H. Zhang, N. Toshima, Catal. Sci. Technol. 3 (2013) 268–278.
[32] G. Sáfrán et al., Microsc. Res. Tech.
[33] Zs Révay, T. Belgya, in: G.L. Molnár (Ed.), Handbook of Prompt Gamma Activation Analysis with Neutron Beams, Kluwer Academic Publishers, Dordrecht/Boston/New York, NY, 2004, ISBN 978-1-4020-1304-1, pp. 1–30.
[34] L. Szentmiklósi, T. Belgya, Zs. Révay, Z. Kis, J. Radioanal. Nucl. Chem. 286 (2010) 501–505, http://dx.doi.org/10.1007/s10967-010-0765-4.
[35] Zs. Révay, T. Belgya, G.L. Molnár, J. Radioanal. Nucl. Chem. 265 (2005) 261–265.
[36] Zs. Révay, Anal. Chem. 81 (2009) 6851–6859, http://dx.doi.org/10.1021/ac9011705.
[37] Zs. Révay, R.B. Firestone, T. Belgya, G.L. Molnár, in: G.L. Molnár (Ed.), Handbook of Prompt Gamma Activation Analysis with Neutron Beams, Kluwer Academic Publishers, Dordrecht/Boston/New York, NY, 2004, ISBN 978-1-4020-1304-1, pp. 173–364.
[38] X. Liu, J. Luo, J. Zhu, Nano Lett. 6 (3) (2006) 408–412.
[39] I. Chakraborty, D. Carvalho, S.N. Shirodkar, S. Lahiri, S. Bhattacharyya, R. Banerjee, U. Waghmare, P. Ayyub, J. Phys.: Condens. Matter 23 (2011) 325–401.
[40] F. Ernst, M.W. Finnis, D. Hofmann, T. Muschik, U. Schönberger, U. Wolf, M. Methfessel, Phys. Rev. Lett. 69 (1992) 620–623.
[41] P. Taneja, R. Banerjee, P. Ayyub, R. Chandra, G.K. Dey, Phys. Rev. B: Condens. Matter 64 (2001) (033 405).
[42] A. Singh, A. Ghosh, J. Phys. Chem. C 112 (2008) 3460–3463.
[43] C. Liang, K. Terabe, T. Hasegawa, M. Aono, Jpn. J. Appl. Phys. 45 (2006) 6046–6048.
[44] C.C. Yang, S. Li, J. Phys. Chem. C 112 (2008) 16400–16404.
[45] Ting-Kai Huang, Tzu-Hou Cheng, Ming-Yu Yen, Wei-Han Hsiao, Lung-Shen Wang, Fu-Rong Chen, Ji-Jung Kai, Chi-Young Lee, Hsin-Tien Chiu, Langmuir 23 (2007) 5722–5726.
[46] A. Sárkány, O. Geszti, G. Sáfrán, Appl. Catal., A: Gen. 350 (2008) 157–163.
[47] T. Shibata, B.A. Bunker, Z. Zhang, D. Meisel, C.F. Vardeman II, J.D. Gezelter, J. Am. Chem. Soc. 124 (2002) 11989–11996.
[48] H. Yasuda, H. Mori, M. Komatsu, K. Takeda, J. Appl. Phys. 73 (1993) 1100–1103.
[49] H. Yasuda, H. Mori, Phys. Rev. Lett. 69 (1992) 3747–3750.
[50] H. Yasuda, H. Mori, Philos. Mag. A 73 (1996) 567–573.
[51] H. Mori, H. Yasuda, Mater. Sci. Eng., A 217/218 (1996) 244–248.
[52] V. Abdelsayed, K.M. Saoud, M. Samy El-Shall, J. Nanopart. Res. 8 (2006) 519–531.
[53] M.P. Mallin, C.J. Murphy, Nano Lett. 2 (11) (2002) 1235–1237.
[54] P. Mulvaney, Langmuir 12 (1996) 788–800.
[55] S.W. Verbruggen, M. Keulemans, J.A. Martens, S. Lenaerts, J. Phys. Chem. C 117 (2013) 19142–19145.
[56] S. Karski, I. Witońska, J. Rogowski, J. Gołuchowska, J. Mol. Catal. A: Chem. 240 (2005) 155–163.
[57] D.I. Kondarides, X.E. Verykios, J. Catal. 158 (1996) 363–377.
[58] M. Boronat, A. Corma, Dalton Trans. 39 (2010) 8538–8546.
[59] B. Hvolbaek, T.V.W. Janssens, B.S. Clausen, H. Falsig, C.H. Christensen, J.K. Norskov, Nano Today 2 (4) (2007) 14–18.
[60] X. Deng, B.K. Min, A. Guloy, C.M. Friend, J. Am. Chem. Soc. 127 (2005) 9267–9270.
[61] W.G. Ferrier, Acta Cryst. 13 (1960) 678–679.
[62] B.N. Zope, D.D. Hibbitts, M. Neurock, R.J. Davis, Science 330 (2010) 74–78.
[63] T. Mallat, A. Baiker, Chem. Rev. 104 (2004) 3037–3058.
[64] K. Goszner, H. Bischof, J. Catal. 32 (1974) 175–182.